Nanoscale

Stabilizing the B-site Oxidation State in ABO3 Perovskite Nanoparticles

Journal:	*Nanoscale*
Manuscript ID	NR-ART-05-2019-004155.R1
Article Type:	Paper
Date Submitted by the Author:	29-Jun-2019
Complete List of Authors:	Ofoegbuna, Tochukwu; Louisiana State University, Darapaneni, Pragathi; Louisiana State University, Cain Department of Chemical Engineering Sahu, Smriti; Louisiana State University Plaisance, Craig; Louisiana State University Dorman, James; Louisiana State University, Chemical Engineering

ARTICLE

Stabilizing the B-site Oxidation State in ABO_3 Perovskite Nanoparticles

Received 00th January 20xx,
Accepted 00th January 20xx

DOI: 10.1039/x0xx00000x

Tochukwu Ofoegbuna,[a] Pragathi Darapaneni,[a] Smriti Sahu,[a] Craig Plaisance [a] and James A. Dorman *[a]

The stabilization of the B-site oxidation state in ABO_3 perovskites using wet-chemical methods is a synthetic challenge, which is of fundamental and practical interest for energy storage and conversion devices. In this work, defect-controlled (Sr-deficiency and oxygen vacancies) strontium niobium (IV) oxide ($Sr_{1-x}NbO_{3-\delta}$, SNO) metal oxide nanoparticles (NPs) were synthesized for the first time using a low-pressure wet-chemistry synthesis. The experiments were performed under reduced oxygen partial pressure to prevent by-product formation and with varying Sr/Nb molar ratio to favor the formation of Nb^{4+} pervoskites. At a critical Sr to Nb ratio (Sr/Nb = 1.3), a phase transition is observed forming an oxygen-deficient $SrNbO_3$ phase. Structural refinement on the resultant diffraction pattern shows that the SNO NPs consists of a near equal mixture of $SrNbO_3$ and $Sr_{0.7}NbO_{3-\delta}$ crystal phases. A combination of Rietveld refinement and X-ray photoelectron spectroscopy (XPS) confirmed the stabilization of the 4+ oxidation state and the formation of oxygen vacancies. The Nb local site symmetry was extracted through Raman spectroscopy and modeled using DFT. As further confirmation, the particles demonstrate the expected absorption highlighting their restored optoelectronic properties. This low-pressure wet-chemical approach for stabilizing the oxidation state of a transition metal has the potential to be extended to other oxygen sensitive, low dimensional perovskite oxides with unique properties.

1. Introduction

Controlling the oxidation state of B-site cations in ABO_3 (A = rare earth or alkaline-earth metal, B = transition metal) perovskites is of fundamental interest for novel phenomena such as metal-insulator transitions,[1, 2] two-dimensional electron/hole gas,[3] and plasmon resonance[4, 5] which are technologically significant for future energy storage and conversion devices.[6, 7] Among various perovskite oxides, the family of strontium niobates ($Sr_{1-x}Nb_{1-y}O_{3\pm\delta}$, SNO) has attracted widespread interest for (opto)electronic applications[8-10] owing to their dynamic (electron mobility, carrier density, and electrical resistivity) and static (absorption, refractive index, and loss function) properties at room temperature.[4, 11] Additionally, the isostructural nature of SNO with strontium titanate ($SrTiO_3$, STO) makes them an exciting class of materials to probe for unique optical,[12] magnetic,[13] and electronic[14] properties. For example, stoichiometric SNO thin films were found to possess high electrical conductivity (3.55×10^4 Ω^{-1} cm^{-1} at room temperature).[11] Alternatively, SNO thin films have been reported to have ferroelectric[15] or plasmonic[4, 5] properties based on the oxygen stoichiometry. SNO nanoparticles (NPs) exhibit distinct physical and chemical properties[16-18] from its thin film counterparts which makes their study critical for the incorporation of unique electronic and optical properties. For this reason, strontium niobate NPs with majority Nb^{5+} oxidation states (i.e. $Sr_2Nb_2O_7$, $SrNb_2O_6$, $Sr_5Nb_4O_{15}$, etc.) have been effectively synthesized via solution-based routes.[16-18] These wet-chemical approaches provide a low-cost method to prepare SNO NPs with various photophysical properties, which can be leveraged to design highly efficient photocatalysts.[16] Although it has been previously shown that Nb^{4+} is naturally stabilized in $BaNbO_3$[19, 20] due to the low enthalpy of formation,[21] the stabilization of Nb^{4+} in SNO remains a synthetic challenge using wet chemistry.[16-18, 22-24] Therefore, the current work reports a facile wet-chemical synthesis method for the preparation of Nb^{4+}-stabilized strontium niobate NPs for the first time.

In this work, a low-pressure wet-chemical synthesis route was employed to form defect-controlled (Sr-deficiency and oxygen vacancies) $Sr_{1-x}NbO_{3-\delta}$ (SNO) nanocrystals. This synthetic route limits available oxygen during the crystallization process allowing for systematic control of oxygen vacancies and thereby modifying the structural, optical, and electronic properties. The elemental composition and crystal structure of the as-synthesized SNO crystals were

[a] Cain Department of Chemical Engineering, Louisiana State University, Baton Rouge, Louisiana 70803, United States.
Email: jamesdorman@lsu.edu.

†Electronic Supplementary Information (ESI) available: TEM/ EDX, complete XRD pattern for $Sr_{1-x}NbO_{3-\delta}$, survey and deconvoluted XPS spectra, schematic representation of the $Sr_{1-x}NbO_{3-\delta}$ crystal, FTIR spectra for $Sr_{1-x}NbO_{3-\delta}$ crystal, XRD pattern and UV-Vis spectra for H_2/Ar annealed samples, ICP-OES analysis, refined atomic coordinates and structural parameters from GSAS II, detailed calculation for oxygen deficiency (δ) from Rietveld refinement and XPS analysis, comparison of experimental Raman spectrum and $SrTiO_3$ phonon frequencies, and calculation of δ from iodometric titration. See DOI: 10.1039/x0xx00000x

studied using energy-dispersive X-ray (EDX) spectroscopy and X-ray diffraction (XRD). The Sr/Nb molar ratio was varied to shift product formation toward SNO and at a critical concentration (Sr/Nb=1.3), a phase transition was observed through the enrichment of the Sr-deficient ($Sr_{0.7}NbO_{3-\delta}$) phase driving the formation to a stoichiometric ($SrNbO_3$) phase. Changes in the Nb-O bond length and phase quantification were determined from structural refinement. X-ray photoelectron spectroscopy (XPS), Raman spectroscopy, and Density Functional Theory (DFT) corroborate these results by confirming the formation of octahedrally coordinated Nb^{4+}. These results suggest that the crystallization of SNO NPs under low oxygen partial pressures and with excess Sr can stabilize Nb^{4+}. Finally, the expected optoelectronic response was observed (UV-Vis spectroscopic) demonstrating the control of structural properties of the material. While this ability to synthetically stabilize the oxidation state of a transition metal in a perovskite matrix provides new insights into the understanding of coordination chemistry[25] in metal oxides, it also enables innovative opportunities for these nanomaterials in advance optoelectronic applications such as plasmonic photocatalysis[5] and perovskite solar cells.[26]

2. Experimental

2.1 Synthesis of Strontium Niobate ($Sr_{1-x}NbO_{3-\delta}$, SNO) Nanocrystals

SNO NPs were synthesized via a two-step co-precipitation/molten salt synthesis[27] under varying pressures. In the first step, the precursor was prepared by dissolving niobium (V) chloride ($NbCl_5$, Alfa Aesar, 99.0% metals basis) into 200 mL of deionized water under vigorous magnetic stirring. Strontium nitrate ($Sr(NO_3)_2$, Alfa Aesar, 99.0%, ACS grade) was then added to the above solution with Sr/Nb mol ratios of up to 1.3 to control the crystal formation. For example, 1.25 mmol of niobium (V) chloride and 1.50 mmol strontium nitrate were added to the precursor solution to prepare a 1.2:1 molar ratio of Sr to Nb. Ammonium hydroxide (NH_4OH, 28-30%, ACS grade), acting as the chelating agent,[28] was added dropwise into the solution until a pH of 9.5 was maintained. After stirring for 2 h, the white precipitate was filtered and washed several times with deionized water before drying overnight at 100 °C. Next, the as-prepared powder was ground with a eutectic molar ratio of $NaNO_3$ (high purity grade, VWR Amresco, 99.0%) and KNO_3 (ACS grade, VWR Amresco) to form a homogeneous powder. The mixture was then transferred to a porcelain boat and heated in a tube furnace at 600 °C under varying total pressure (0.2 – 760 Torr) for 2 h. After cooling, the resultant powder is washed several times with deionized water and dried overnight at 100 °C to obtain SNO nanocrystals.

2.2 Characterization

The SNO nanoparticle sizes and structure were determined by transmission electron microscopy (TEM) using a JEOL JEM-1400 operating at an accelerating voltage of 120 kV. TEM images were collected using a Gatan Orius 2k x 2k CCD camera. The powder sample was dispersed in toluene and drop casted on a lacey carbon type-A, 300 mesh copper grid prior to imaging.

The elemental composition of the SNO NPs was determined using a FEI Quanta 3D FIB microscope equipped with an EDAX Apollo XL EDX detector operating at an accelerating voltage of 20 kV and a current of 4 nA. The working distance was maintained at ~10 mm. The samples were dried overnight on carbon tape and then sputtered with Pt for 5 min to limit charging.

The crystal structure was identified by performing powder XRD using PANalytical X-ray diffractometer operating at 45 kV and 40 mA. The θ-2θ radial scan was performed over the range 5-70º with a step size of 0.04º and dwell time of 60 s, using Cu K_α (λ=1.54 Å) as radiation source. Rietveld refinement was performed on the resultant diffraction pattern using the GSAS II software[29] for phase quantification. Full structural refinement was achieved via the refinement of the following: structural parameters (histogram scale factor, atomic coordinates, and isotropic atomic displacement parameter), cell parameters, peak shape parameters (Cagliotti parameters, sample displacement, phase fraction, size, and microstrain), and background parameters (10-coefficient log interpolate polynomial).[30, 31]

The oxidation states of the SNO NPs were determined from XPS measurements performed using a Scienta Omicron ESCA 2SR XPS system equipped with a monochromatic Al K_α ($h\nu$=1486.6 eV) X-ray source and a hemispherical analyzer with a 128-channel detector. The inherent gaussian width of the photon source was 0.2 eV. The pressure inside the chamber was maintained at 1.5×10^{-9} Torr. The XPS spectra were calibrated to adventitious C 1*s* peak at 284.6 eV. All peaks were fit (using CasaXPS software[32]) to symmetric Voigt functions (70% Gaussian and 30% Lorentzian) and a Shirley background to determine peak positions and areas. The fitting parameters were generated with a Levenberg-Marquardt optimization algorithm. Niobium (V) oxide (Nb_2O_5, Alfa Aesar, 99.95% metals basis) powder was used as a reference for oxidation state confirmation.

Raman spectroscopy was performed via a Renishaw inVia Reflex Raman Spectrometer with a 0.05 mW diode laser at an excitation wavelength of 532 nm, exposure time of 0.5 s, and spectral resolution of 1 cm^{-1}. The diameter of the focused laser spot on the sample at 50x magnification was approximately 5 µm. Three scans were averaged to obtain the reported spectra. For peak deconvolution, the background was subtracted from the resulting spectra to resolve the active modes.

The absorption spectra of the SNO NPs were recorded using a Perkin-Elmer Lambda 900 UV/Vis/NIR spectrometer equipped with an integrating sphere and a center mounted sample holder. A 30 W deuterium and 100 W halogen lamp were used for UV and visible-IR light irradiation, respectively. The absorption scans ranging from 250 to 800 nm were obtained using a scan rate of 1 nm/s with no monochromator change. The powder samples were dried onto a glass substrate to perform UV-Vis measurements.

2.3 Ab Initio Calculations

Planewave density functional theory (DFT) calculations were performed using the Vienna Ab-Initio Simulation Package (VASP)[33, 34] to analyze the characteristics observed in the SNO

(Sr/Nb = 1.3) Raman spectrum. These calculations used the Perdew–Burke–Ernzerhof (PBE) functional[35] to account for exchange and correlation and the projector augmented wave (PAW) method[36] to describe wave functions in the atomic core regions. All calculations were performed with a plane-wave cutoff energy of 396 eV and a 4×4×4 Γ-centered k-point grid. A 2×2×2 supercell was used for all calculations with the experimentally determined unit cell lattice parameter of 4.042 Å. Prior to computing force constants, the atomic positions in the supercell were optimized until the force on each atom was less than 0.05 eV/Å. Force constants were calculated using the finite difference method with a displacement of 0.01 Å. The Phonopy package[37] was used to calculate phonon densities of states based on the obtained force constants.

3. Results and discussion

Strontium niobate ($Sr_{1-x}NbO_{3-\delta}$, SNO) nanocrystals were synthesized with equimolar Sr to Nb precursor ratios using the two-step co-precipitation/pressure-controlled molten salt synthesis procedure. In this synthetic method, a single-source amorphous complex precursor is prepared in the co-precipitation step and the subsequent molten-salt step promotes the crystallization of the amorphous precipitate by providing a low melting point salt solvent to facilitate the diffusion of reacting species.[27] The XRD diffraction peaks (Fig. 1) for the $Sr_{1-x}NbO_{3-\delta}$ nanocrystals were indexed to the cubic phase of $Sr_{0.7}NbO_3$ with space group *Pm-3m* (ICDD 19-2410) and lattice parameter a = 3.981 Å. Additionally, low intensity shoulder peaks are observed on the main diffraction peaks due to the crystallization of a secondary lattice. The (110) reflection is presented on the right to highlight these low intensity shoulder peaks which have been indexed to the $NaNbO_3$ (ICDD 19-1221) crystal structure. The remaining diffraction peaks, indicated by asterisks, are due to an unknown secondary phase partially matching with $SrNb_6O_{16}$ (ICDD 46-1287) and (K, Na)$SrNbO_x$-based complexes.[38-42] In either case, the defect structures will be referred to as Nb^{5+} crystal due to the presence of this oxidation state. The observed Nb^{5+} crystal lattices are formed due to the thermodynamically stable pentavalent state which can be prevented by reducing the oxygen partial pressure during the reaction.[43] Therefore, an analogous approach was implemented with a molten salt solvent under reduced oxygen atmospheres to shift the thermodynamic equilibrium to Nb^{4+}, as seen in Fig. 1. While diffraction peaks associated with $NaNbO_3$ are not observed at lower oxygen partial pressures, diffractions for Nb^{5+}-based crystals remain. These results indicate that $NaNbO_3$ is formed directly from the oxidation of niobium in an oxygen-rich environment whereas the Nb^{5+}-based impurities are formed by the oxidation of niobium during the co-precipitation step.[27] TEM images of the resultant particles (Fig. S1a, ESI†) show NPs with sizes ranging from roughly 10 to 20 nm, confirming the calculated crystallite size

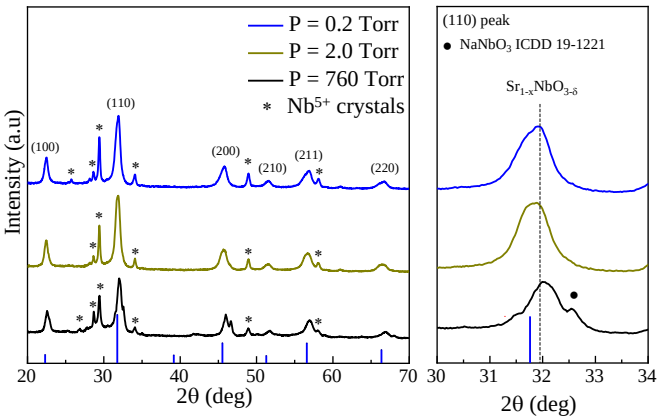

Fig. 1 Pressure dependence of $Sr_{1-x}NbO_{3-\delta}$ (Sr/Nb=1.0) nanoparticles for 0.2, 2.0, and 760 Torr. The $NaNbO_3$ reflection is highlighted in the expanded view (circle). The asterisks indicate reflections from Nb stabilized in the 5+ state. The dashed lines are a guide to the eye for $Sr_{0.7}NbO_{3-\delta}$ (ICDD 19-2410, blue vertical marker) phase identification.

from XRD. The corresponding EDX spectrum, shown in Fig. S1b (ESI†), confirms the presence of Sr, Nb, and O in the nanocrystals along with Na and K from the Nb^{5+} crystals.

In order to prevent the oxidation within the co-precipitation step, non-stoichiometric A/B ratios have been employed to manipulate crystallization kinetics.[44-46] To verify this effect during initial A-O-B bond formation, excess Sr was incorporated into the reaction mixture at reduced pressures (0.2 Torr) to inhibit the formation of unsaturated Nb^{4+} during precipitation. With increasing Sr content, a Sr-deficient to stoichiometric phase transition is observed (Fig. 2) and indexed to cubic $SrNbO_3$ with space group *Pm-3m* (ICDD 6-3450, a = 4.040 Å). A magnified view of the (110) reflection peak

Table 1 Comparison of the Lattice Parameters and Crystallite Size for $Sr_{1-x}NbO_{3-\delta}$ Nanoparticles Determined from Concentration Control Studies

Sr/Nb Ratio	Lattice Parameter (Å)	Crystallite Size (nm)
1.0	3.966	10.26 ± 2.79
1.2	3.962	10.97 ± 2.43
1.3	3.970	8.61 ± 3.51

highlights the shift in peak position upon Sr-enrichment. The lattice parameters and crystallite sizes were extracted for each composition (Table 1). The Sr-deficient phase was indexed to cubic $Sr_{0.7}NbO_3$ with the calculated lattice parameter matching the reported literature value (a = 3.981 Å).[42] For the 1.3 molar ratio (Table 2), the stoichiometric phase is similar to those reported for thin films (4.042 Å),[47] with a crystallite size of approximately 16 nm. Furthermore, quantitative composition analysis was performed on the 1.3 molar ratio sample using

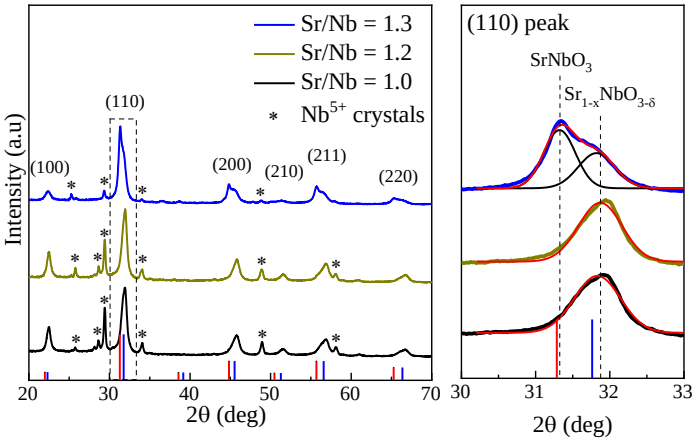

Fig. 2 Concentration dependence of $Sr_{1-x}NbO_{3-\delta}$ (Sr/Nb =1.0, 1.2, and 1.3) nanoparticles synthesized under total pressure of 0.2 Torr. The dashed lines are a guide to the eye for $SrNbO_3$ (ICDD 6-3450, red vertical marker) and $Sr_{0.7}NbO_{3-\delta}$ (ICDD 19-2410, blue vertical marker) phase identification.

inductively coupled plasma optical emission spectrometry (ICP-OES). The as-determined Sr (49 mol%) and Nb (51 mol%) ratios agree with the theoretical $Sr_{0.7}NbO_{3-\delta}/SrNbO_3$ stoichiometry (Table S1, ESI†). These results demonstrate that the new low-pressure molten salt synthesis method results in Sr-deficient ($Sr_{0.7}NbO_3$) and stoichiometric ($SrNbO_3$) phases.

Incorporating excess Sr into the synthesis limits the formation of Nb^{5+} crystals as seen by the reduced defect peak intensity (Fig. 2). Similar growth kinetics has been observed for the conversion of (wurtzite) InP to (zinc blende) $Ga_xIn_{1-x}P$ nanowires.[48, 49] Ga is incorporated into the In occupied tetrahedral sites of the InP crystal in order to favor the formation of the zinc blende structure. In the presence of excess In, the diffusion of Ga into the crystal was inhibited, resulting in the formation of Ga-deficient nanowires with wurtzite structure. Based on the previously reported structure transition, the diffraction data indicates that the increased Sr/Nb molar ratio prevents the diffusion of Na^+/K^+ into the crystal. Next, the vacant Sr-sites begin to be occupied at higher Sr^{2+} concentrations, leading to the formation of stoichiometric $SrNbO_3$. However, when the Sr^{2+} concentration is increased above the 1.3 molar ratio, the Sr-deficient lattice and Nb^{5+} crystals are reformed (Fig. S2, ESI†). Therefore, it is important to maintain a critical Sr concentration to stabilize a majority Nb^{4+} by limiting the formation of Nb^{5+} crystals.

To quantify the ratio of stoichiometric and Sr-deficient phases present in the SNO (Sr/Nb = 1.3) NPs, Rietveld refinement was performed. The diffraction pattern was refined using the cubic space group *Pm-3m* (no. 221) $SrNbO_3$[47] and $Sr_{0.7}NbO_3$[42] as structural models for the stoichiometric and Sr-deficient phases, respectively. Other strontium niobate stoichiometries (not included) were considered but resulted in poor fits ($\chi^2 > 5$). Since the aim of the structural refinement was to quantify the SNO phases, the reflections due to the

Table 2 Comparison of the Lattice Parameters and Crystallite Size for $Sr_{1-x}NbO_{3-\delta}$ (Sr/Nb = 1.3) Phases

Sr/Nb = 1.3	Lattice Parameter (Å)	Crystallite Size (nm)
Sr-deficient phase	3.970	8.61 ± 3.51
Sr-rich phase	4.042	16.41 ± 6.76

Nb^{5+}-based crystals were excluded from the final structural refinement. However, it was possible to obtain good structural agreement (R_p = 3.65%, R_{wp} = 4.47%, and χ^2 = 2.64) even when the Nb^{5+}-based reflections were included. A summary of the crystallographic data and final refinement details are listed in Table 3. The fits were deemed to be good based on these parameters coupled with visual confirmation from Fig. 3a and 3b. The refined atomic coordinates and structural parameters are provided in Table S2 of the Supporting Information with

Table 3 Crystallographic Data and Refined Lattice Parameters for $Sr_{1-x}NbO_{3-\delta}$ (Sr/Nb = 1.3) Phases based on X-ray Diffraction Data

Parameters	$SrNbO_3$	$Sr_{0.7}NbO_3$
wavelength (Å)	1.541	
temperature (K)	300	
2θ range (°)	20-70	
space group	*Pm-3m* (No. 221)[a]	*Pm-3m* (No. 221)[b]
a, b, c (Å)	4.042(7)	3.982(7)
α, β, γ (°)	90	90
V (Å^3)	66.075	63.176
Z	1.0	
goodness-of-fit	1.73	

[a-b] space group ref.: ICDD 6-3450, ICDD 19-2410

the lattice parameters for the refined phases determined to be 4.042(7) Å and 3.982(7) Å (Table 3). Both structural parameters show good agreement with previous studies.[42, 47]

From the refined crystal structure, the amount of $SrNbO_3$ and $Sr_{0.7}NbO_3$ is estimated to be 53 and 47 wt% respectively. The schematic drawing in Fig. 3c highlights the effect of the phase transition on the Nb octahedral coordination environment (NbO_6). In the $SrNbO_3$ phase the Nb-O bond length is 2.02 Å, while in the defective phase the bond length is reduced to 1.99 Å. The contraction in bond length is attributed to the larger B-site oxidation state of A-site deficient ABO_3 perovskites.[50, 51] For $Sr_{1-x}NbO_3$, the reduced Sr vacancy lowers the Nb oxidation state, allowing for the unit cell to expand as observed in the crystal refinement.[51, 52] It is also important to highlight that in the refinement, the occupancy of the anion sites for the Sr-deficient phase were kept unchanged to represent the $Sr_{0.7}NbO_3$ (40% Nb^{5+}) stoichiometry. Therefore, the resultant diffraction pattern could be accurately captured by this approach, which ignores the formation of

oxygen vacancies (δ)[53] and possible phase transformations due to high vacancy concentrations.[54]

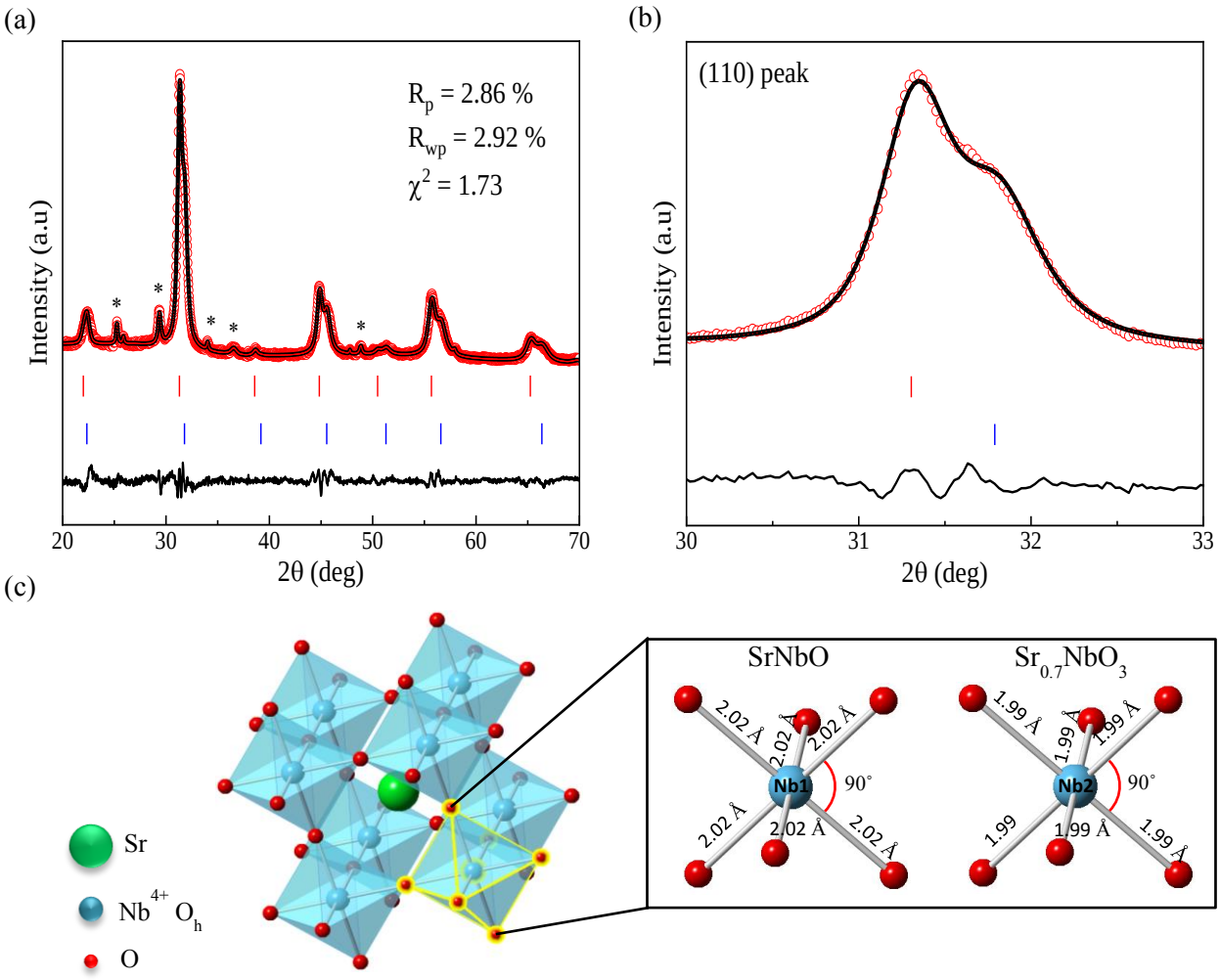

Fig. 3 (a) XRD pattern and Rietveld refinement for $Sr_{1-x}NbO_{3-\delta}$ (Sr/Nb=1.3) nanoparticle recorded at room temperature with λ = 1.541 Å. The upper symbols illustrate the observed data (circles) and the calculated pattern (solid line). The vertical markers show calculated positions of Bragg reflections. The red and blue vertical marks indicate the Bragg peak positions of $SrNbO_3$ (wt = 52.96%) and $Sr_{0.7}NbO_3$ (wt = 47.04%) respectively. The lower curve represents the difference between observed and calculated intensities. Impurity peaks are indicated in asterisks and were excluded from the refinement. (b) enlarged XRD pattern showing fit for (110) peak. (c) Illustration of refined crystal structure and Nb coordination environments.

To corroborate the $Sr_{1-x}NbO_{3-\delta}$ crystal structures identified by diffraction studies, the oxidation states of Sr, Nb, and O in the SNO (Sr/Nb=1.3) NPs were determined using XPS (Fig S3 and 4). Peaks associated with the Sr 3*d*, Nb 3*d*, and O 1*s* states are identified in the XPS survey scan (Fig. S3a, ESI†). The detailed scan of the Sr 3*d* region (Fig. S3b, ESI†) shows two sharp peaks around 132.8 eV (Sr $3d_{5/2}$) and 134.6 eV (Sr $3d_{3/2}$) corresponding to Sr^{2+}.[55] The Nb ($3d_{5/2}$ and $3d_{3/2}$) peaks, Fig. 4a, of the as-synthesized SNO NPs are located at lower binding energies compared to the Nb_2O_5 (Nb^{5+}) reference powder. Deconvolution of the Nb 3*d* spectrum shows the presence of two oxidation states (Fig. S3c, ESI†) with the higher energy state at 206.5 eV (Nb $3d_{5/2}$) and 209.3 eV (Nb $3d_{3/2}$) corresponding to Nb^{5+} (~23%), as expected due to charge neutrality. These peak positions differ from the reference Nb_2O_5 by ~0.2 eV, which is within the resolution of the instrument, suggesting a good agreement between the deconvoluted and reference spectra. Furthermore, the majority species (~77%) is lower in energy (206.2 eV and 209.0 eV), in agreement with reported Nb^{4+} structures.[56-60] The deconvoluted O 1*s* spectra (Fig. 4b and S3d) identifies four peaks located at 529.2 (SNO lattice),[55, 59] 530.0 ($Sr_{0.7}NbO_{3-\delta}$ lattice),[46] 531.2 (surface OH),[61] and 532.0 eV (nearby oxygen vacancies).[62] As such, an oxygen vacancy of δ~0.35 can be extracted from both XPS and refinement data (Table S3) and is

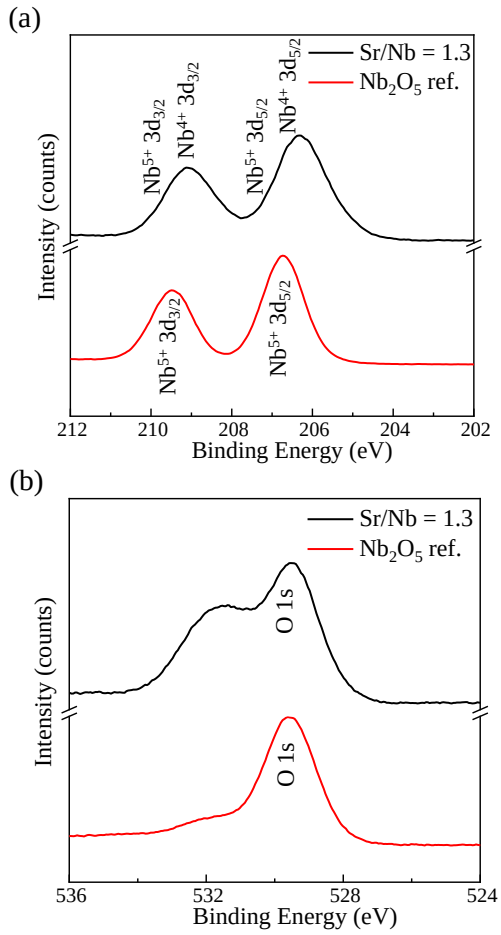

Fig. 4 X-ray photoelectron spectra for $Sr_{1-x}NbO_{3-\delta}$ (Sr/Nb=1.3) NPs synthesized under total pressure of 0.2 Torr: (a) Nb 3*d* spectrum and (b) O 1*s* spectrum. Nb_2O_5 (red) is plotted as an oxidation state reference.

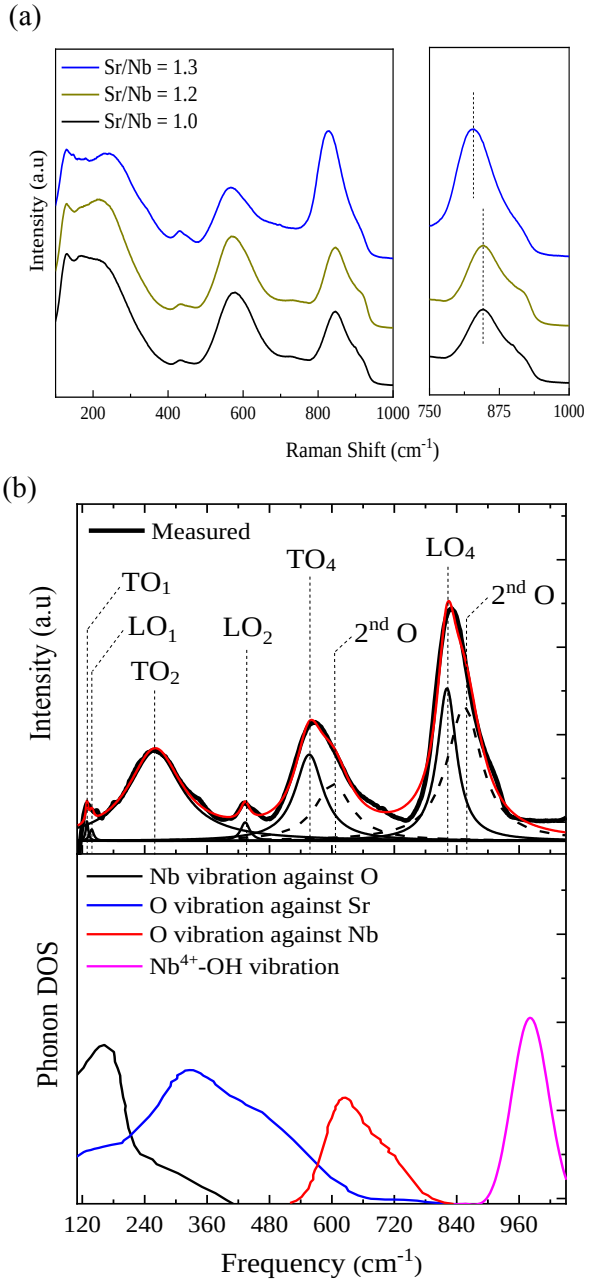

Fig. 5 (a) Normalized Raman spectra for $Sr_{1-x}NbO_{3-\delta}$ (Sr/Nb=1.0, 1.2, and 1.3) NPs with an expanded view to highlight red shift in F_{1u} peak position and intensity enhancement. (b) spectral deconvolution of Sr/Nb = 1.3 and simulated partial phonon density of states.

in agreement with literature.[42] This value of δ was further verified analytically by performing three parallel iodometric titrations[63, 64] (detailed calculations are described in the ESI†). Based on these titrations, a δ of ~0.37±0.06 was calculated, within 3% of the previously determined value (~0.35). These results point to the fact that vacancy formation is necessary to maintain charge neutrality within the $Sr_{0.7}NbO_{3-\delta}$ lattice.[51, 53, 65]

To verify octahedral (O_h) site symmetry around Nb^{4+}, Raman spectra were collected for the SNO samples (Fig. 5a). Despite crystals with cubic symmetry (*Pm-3m)* not expected be Raman active, symmetrically forbidden modes have been observed in analogous structures (STO) due to octahedron distortions.[44, 66-69] Five characteristic peaks, positioned at ~130, 250, 430, 560, and 830 cm^{-1}, have been deconvoluted and assigned to different transverse (TO) and longitudinal (LO) optic modes (Fig. 5b and Table S4).[44, 66, 67] Furthermore, no shift in peak position is seen with an increase in molar ratio from 1.0 to 1.2 suggesting that the excess Sr^{2+} is not incorporated into the $Sr_{1-x}NbO_{3-\delta}$.[45] At the higher Sr/Nb ratio, the higher frequency peak red-shifts and this is attributed to the formation of stoichiometric $SrNbO_3$.[70] Furthermore, the enhancement of the ~830 cm^{-1} peak intensity relative to the peak positioned at ~560 cm^{-1} is due to surface structure effects.[67, 68, 71] These results in conjunction with the previously presented XPS analysis demonstrate that Nb^{4+} is locked into O_h coordination.

Partial phonon density of states (DOS) calculations were performed to provide a geometrical description of the

vibrational modes responsible for the experimentally observed peaks in the Raman spectrum. A lattice parameter of 4.042 Å, which is consistent with the experimentally determined lattice parameter (Table 2), was used for the optimized cubic (space group *Pm-3m*) SNO supercell. The schematic illustrated in Fig. S4 (ESI†) shows that the atomic structure of the SNO nanoparticle is composed of point defects in the bulk and hydroxyl groups on the surface. Therefore, to determine the bulk vibrational frequencies, an atomic cell with point defects (Sr or O vacancy) was simulated (not shown). According to these calculations, the phonon mode positioned at 162 cm^{-1} corresponds to Nb motion against O vibrations in the presence of an O vacancy and the calculated peak at 326 cm^{-1} involves the vibrations of O ions against Sr cation in the presence of a Sr vacancy. The final peak positioned at 626 cm^{-1} is attributed to O vibration against Nb ions in the presence of an O vacancy. Furthermore, in order to mirror the nanoparticle surface observed from XPS and FTIR spectroscopy (Fig. S3 and S5), surface calculations were performed using a defect-free cubic $SrNbO_3$ cell with terminal niobium atoms bonded to hydroxyl groups (Nb^{4+}-OH) resulting in a Raman active mode at 981 cm^{-1}. The deviation from experiment is ascribed to a simplified representation of the NbO_x-OH on the nanoparticle surface modeled by DFT as described in literature.[71-73] This calculation shows that the highest wavenumber band originates from the stretching of the Nb-O bond in hydroxyl activated NbO_6 octahedra. Overall, these first-principles calculations demonstrate that the observed Raman activity for these nanocrystals is due to a combination of surface effects and point defects. As such, these DFT and Raman results highlight the presence of vibrational modes consistent with a perovskite structure for these Nb^{4+} stabilized SNO NPs.

To probe the optical response of the SNO nanocrystals, UV-Vis absorption measurements were performed on the synthesized powders. The absorption spectra (Fig. 6) shows no visible absorption upon Sr-enrichment despite the formation of $Sr_{1-x}NbO_{3-\delta}$ (x = 0 and 0.3) as seen visually. However, literature reports a shift from red/bronze for stoichiometric SNO which shifts to blue/black with decreasing Sr concentrations (x= 0.3).[4, 42] Therefore, the white color of these SNO NPs is attributed to the presence of low levels of Nb^{5+} within the crystal and contribute to the observed insulating nature.[2, 4, 51] In order to reduce the Nb^{5+} crystals, the as-synthesized SNO (Sr/Nb=1.3) NPs were annealed under H_2/Ar atmosphere at 800 °C. The resulting powders have a dark grey appearance and an enhanced optical absorption in the visible region (Fig. 6). Moreover, the resultant diffraction pattern for the annealed sample shows the SNO crystal with significantly reduced Nb^{5+} reflections (Fig. S6, ESI†). For comparison, the SNO (Sr/Nb=1.0) NPs were annealed in reducing atmospheres and similar reductions to the Nb^{5+} reflections are observed (Fig. S7a, ESI†), however, there is no significant change to the nanoparticle absorbance (Fig. S7b, ESI†). Therefore, it is important to minimize the formation of these Nb^{5+} crystals during the molten salt step to obtain enhanced absorption. Although further investigation is needed to understand the effect of H_2/Ar annealing on the electronic structure, the present results demonstrate the presence of colored SNO nanocrystals.

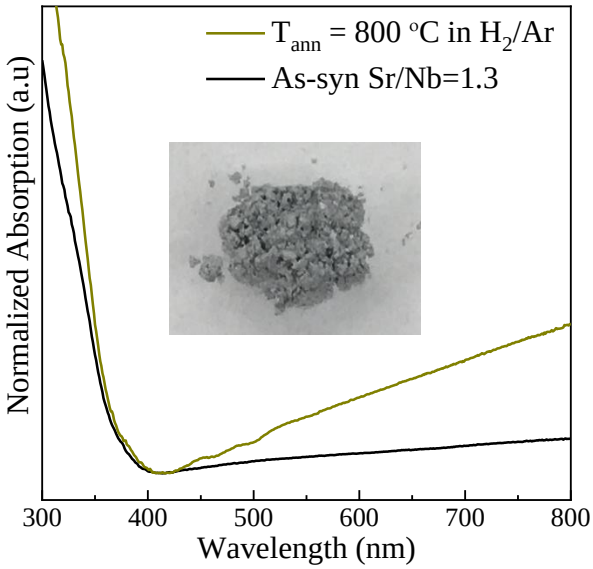

Fig. 6 Optical absorption spectra for as-synthesized and H_2/Ar annealed $Sr_{1-x}NbO_{3-\delta}$ (Sr/Nb=1.3) NPs. The inset shows the dark grey appearance of the particles after H_2/Ar treatment.

The scattering, electronic/optical, and spectroscopic results affirm the formation of SNO (Sr/Nb=1.3) nanocrystals with a quantitatively determined composition of $SrNbO_3$ and $Sr_{0.7}NbO_{2.65}$. From these results, it is also evident that the crystallization is performed by limiting the formation of a Nb^{5+}-based crystal. XPS analysis shows that ~77% of niobium in the nanocrystal is stabilized in the tetravalent oxidation state and ~23% is present in the pentavalent state. Furthermore, the characterization of these NPs points to the formation of octahedrally coordinated niobium with a majority 4+ oxidation state. Unfortunately, the presence of the minority Nb^{5+} species suppress the optoelectronic properties of the as-synthesized NPs. However, after annealing in reducing atmospheres, the expected optoelectronic responses and powder color are restored, as verified by UV-Vis spectroscopy.

4. Conclusions

In summary, SNO NPs with dimensions varying from 10 to 20 nm were synthesized using a two-step co-precipitation/ pressure-controlled crystallization method. The experiments were performed under reduced oxygen partial pressure to remove $NaNbO_3$ formation and the Sr/Nb molar ratio was varied to shift product formation toward SNO and away from Nb^{5+}-based crystals. From initial diffraction studies, a phase transition for the SNO (Sr/Nb=1.3) NPs was observed through the enrichment of the Sr-deficient ($Sr_{0.7}NbO_{3-\delta}$) phase to form a stoichiometric ($SrNbO_3$) phase. Structural refinement on the resultant diffraction pattern shows that the SNO NPs consists of $SrNbO_3$ (wt = 53%) and $Sr_{0.7}NbO_{3-\delta}$ (wt = 47%) crystals. The oxygen-deficiency (δ) in the $Sr_{0.7}NbO_{3-\delta}$ phase was calculated to be ~0.35 based on a combination of XPS and Rietveld refinement. XPS and Raman analysis showed that through the formation of oxygen vacancies, the pentavalent state of

niobium is reduced to the Nb^{4+} valency and, as a result, the observed oxygen vacancies create local distortions in the NbO_6 octahedra. Furthermore, the observed phonon frequencies were compared with density functional theory calculations. The as-synthesized NPs were subsequently annealed in H_2/Ar atmospheres to reduce the Nb^{5+} species responsible for quenching the optoelectronic properties, resulting in a change in the powder color and optical absorption. These results demonstrate that through the stabilization of Nb^{4+}, a bi-phasic SNO nanocrystal is synthesized. This wet-chemical method for stabilizing the oxidation state of a transition metal in an oxygen-controlled environment can be extended to the synthesis of other low- dimensional perovskites to elucidate the structure-property relationship of ABO_3 perovskites for next-generation optoelectronic devices. Ultimately, the demonstrated wet-chemical approach provides a fundamental framework for the synthesis of low-dimensional perovskites, which have the potential to advance the fields of photocatalysis and photovoltaics.

Conflicts of interest

There are no conflicts to declare.

Acknowledgements

T.O. acknowledges the fellowship support from the Louisiana College of Engineering and CHE-1709902 for supplies. P.D. acknowledge the Louisiana Board of Regents (LEQSF(2016-19)-RD-A-03) for financial support. The authors thank Ms. Natalia Moura for her assistance in performing TEM imaging.

Author contribution

T.O. performed the synthesis of the $Sr_{1-x}NbO_{3-\delta}$ nanoparticle samples, and completed the XRD, UV-Vis, XPS, Rietveld refinement, and Raman analysis. P.D. performed the EDX and XPS measurements. S.S. assisted in the Raman analysis. C.P. performed the DFT calculations. J.A.D. conceived the project of stabilizing the Nb^{4+} oxidation state to synthesize $Sr_{1-x}NbO_{3-\delta}$ using wet chemistry.

References

1. J. Seo, Y. Moriya, M. Kodera, T. Hisatomi, T. Minegishi, M. Katayama and K. Domen, *Chem. Mater.*, 2016, **28**, 6869-6876.
2. D. Oka, Y. Hirose, M. Kaneko, S. Nakao, T. Fukumura, K. Yamashita and T. Hasegawa, *ACS Appl. Mater. Interfaces*, 2018.
3. Y. Zhang, B. Feng, H. Hayashi, T. Tohei, I. Tanaka, Y. Ikuhara and H. Ohta, *J. Appl. Phys.*, 2017, **121**, 185102.
4. D. Wan, Y. Zhao, Y. Cai, T. Asmara, Z. Huang, J. Chen, J. Hong, S. Yin, C. Nelson and M. Motapothula, *Nat. Commun.*, 2017, **8**, 15070.
5. D. Wan, B. Yan, J. Chen, S. Wu, J. Hong, D. Song, X. Zhao, X. Chi, S. Zeng and Z. Huang, *Chem. Mater.*, 2019.
6. J. Chen, H. Chen, F. Hao, X. Ke, N. Chen, T. Yajima, Y. Jiang, X. Shi, K. Zhou and M. Döbeli, *ACS Energy Lett.*, 2017, **2**, 915-921.
7. A. Bera, K. Wu, A. Sheikh, E. Alarousu, O. F. Mohammed and T. Wu, *J. Phys. Chem. C*, 2014, **118**, 28494-28501.
8. Y. Nezu, Y.-Q. Zhang, C. Chen, Y. Ikuhara and H. Ohta, *J. Appl. Phys.*, 2017, **122**, 135305.
9. X. Xu, C. Randorn, P. Efstathiou and J. T. Irvine, *Nat. Mater.*, 2012, **11**, 595.
10. Y. Zhu, Y. Dai, K. Lai, Z. Li and B. Huang, *J. Phys. Chem. C*, 2013, **117**, 5593-5598.
11. D. Oka, Y. Hirose, S. Nakao, T. Fukumura and T. Hasegawa, *Phys. Rev. B*, 2015, **92**, 205102.
12. A. Banik, M. S. Ansari, S. Alam and M. Qureshi, *J. Phys. Chem. C*, 2018, **122**, 16550-16560.
13. W. Xu, J. Yang, W. Bai, K. Tang, Y. Zhang and X. Tang, *J. Appl. Phys.*, 2013, **114**, 154106.
14. H. W. Jang, A. Kumar, S. Denev, M. D. Biegalski, P. Maksymovych, C. W. Bark, C. T. Nelson, C. M. Folkman, S. H. Baek, N. Balke, C. M. Brooks, D. A. Tenne, D. G. Schlom, L. Q. Chen, X. Q. Pan, S. V. Kalinin, V. Gopalan and C. B. Eom, *Phys. Rev. Lett.*, 2010, **104**, 4.
15. K. Balasubramaniam, Y. Cao, N. Patel, S. Havelia, P. Cox, E. Devlin, E. Yu, B. Close, P. Woodward and P. Salvador, *J. Solid State Chem.*, 2008, **181**, 705-714.
16. D. Chen and J. Ye, *Chem. Mater.*, 2009, **21**, 2327-2333.
17. I.-S. Cho, S. Lee, J. H. Noh, D. W. Kim, D. K. Lee, H. S. Jung, D.-W. Kim and K. S. Hong, *J. Mater. Chem.*, 2010, **20**, 3979-3983.
18. S. Xie, Y. Wang, Q. Zhang, W. Deng and Y. Wang, *Chem. Commun.*, 2015, **51**, 3430-3433.
19. D. Guo, H. Hua, C. Hu and Y. Xi, *J. Phys. Chem. C*, 2013, **117**, 14281-14288.
20. X. Xie, C. Hu, D. Guo, H. Hua, T. Liu and P. Jiang, *J. Phys. Chem. C*, 2012, **116**, 23041-23046.
21. L. Reznitskii, *Inorg. Mater.*, 2001, **37**, 491-495.
22. O. G. Rojas, G. Song and S. R. Hall, *CrystEngComm*, 2017, **19**, 5351-5355.
23. B. Brahmaroutu, G. L. Messing and S. Trolier-McKinstry, *J. Amer. Ceram. Soc.*, 1999, **82**, 1565-1568.
24. B. Lin, J. Ma, Y. Yao, J. Liu, Y. Ren, X. Jiang, Y. Sun and Z. Liu, *J. Amer. Ceram. Soc.*, 2008, **91**, 1329-1331.
25. Y. M. Kiselev, *Russ. J. Inorg. Chem.*, 2007, **52**, 1717-1725.
26. X. Chen and M. Gu, *ACS Appl. Energy Mater.*, 2019.
27. S. B. Alaparthi, Y. Tian and Y. Mao, *Nanotechnol.*, 2013, **25**, 025703.
28. M. Zhang, H. Liu, Z. Liu, C. Fang and Y. S. Meng, *ACS Appl. Energy Mater.*, 2018.
29. A. Larsson and R. Von Dreele, *Los Alamos, NM: Los Alamos Laboratory*, 1994.
30. D. Neiner, N. L. Okamoto, P. Yu, S. Leonard, C. L. Condron, M. F. Toney, Q. M. Ramasse, N. D. Browning and S. M. Kauzlarich, *Inorg. Chem.*, 2009, **49**, 815-822.
31. H. Rietveld, *J. Appl. Crystallogr.*, 1969, **2**, 65-71.
32. N. Fairley, *CasaXPS Manual 2.3. 15: CasaXPS Processing Software for XPS Spectra*, Casa Software Limited, 2009.
33. G. Kresse and J. Furthmüller, *Phys. Rev. B*, 1996, **54**, 11169.
34. G. Kresse and J. Furthmüller, *Comput. Mater. Sci.*, 1996, **6**, 15-50.
35. J. P. Perdew, K. Burke and M. Ernzerhof, *Phys. Rev. Lett.*, 1996, **77**, 3865.

36. P. E. Blöchl, *Phys. Rev. B*, 1994, **50**, 17953.
37. A. Togo, F. Oba and I. Tanaka, *Phys. Rev. B*, 2008, **78**, 134106.
38. W. Zhang, X. Pan, P. Long, X. Liu, X. Long, Y. Yu and Z. Yi, *J. Mater. Chem. A*, 2017, **5**, 18998-19006.
39. L. Liu, F. Gao, G. Hu and J. Liu, *Powder Technol.*, 2013, **246**, 395-397.
40. A. Lima, J. Sczancoski, M. S. Li, E. Longo and E. Camargo, *Ceram. Int.*, 2016, **42**, 4709-4714.
41. A. Surmin, P. Fertey, D. Schaniel and T. Woike, *Acta Crystallogr. Sect. B: Struct. Sci.*, 2006, **62**, 228-235.
42. D. Ridgley and R. Ward, *J. Amer. Chem. Soc.*, 1955, **77**, 6132-6136.
43. M. J. Campion, H. J. Brown-Shaklee, M. A. Rodriguez, J. J. Richardson, P. G. Clem and J. F. Ihlefeld, *J. Amer. Ceram. Soc.*, 2013, **96**, 743-749.
44. F. A. Rabuffetti, H.-S. Kim, J. A. Enterkin, Y. Wang, C. H. Lanier, L. D. Marks, K. R. Poeppelmeier and P. C. Stair, *Chem. Mater.*, 2008, **20**, 5628-5635.
45. Y. Guo, H. Liu, D. Yu and J.-M. Liu, *Phys. Rev. B*, 2012, **85**, 104108.
46. G. Saint-Girons, R. Bachelet, R. Moalla, B. Meunier, L. Louahadj, B. Canut, A. Carretero-Genevrier, J. Gazquez, P. Regreny and C. Botella, *Chem. Mater.*, 2016, **28**, 5347-5355.
47. T. Tomio, H. Miki, H. Tabata, T. Kawai and S. Kawai, *J. Appl. Phys.*, 1994, **76**, 5886-5890.
48. V. Dagytė, M. Heurlin, X. Zeng and M. T. Borgström, *Nanotechnol.*, 2018, **29**, 394001.
49. S. Lehmann, D. Jacobsson and K. A. Dick, *Nanotechnol.*, 2015, **26**, 301001.
50. B. Dabrowski, O. Chmaissem, P. Klamut, S. Kolesnik, M. Maxwell, J. Mais, Y. Ito, B. Armstrong, J. Jorgensen and S. Short, *Phys. Rev. B*, 2004, **70**, 014423.
51. P. Efstathiou, X. Xu, H. Ménard and J. T. Irvine, *Dalton Trans.*, 2013, **42**, 7880-7887.
52. B. Hessen, S. A. Sunshine, T. Siegrist and R. Jimenez, *Mater. Res. Bull.*, 1991, **26**, 85-90.
53. P. Darapaneni, O. Kizilkaya, Z. Wang and J. A. Dorman, *J. Phys. Chem. C*, 2018, **122**, 22699-22708.
54. D. Marrocchelli, N. H. Perry and S. R. Bishop, *Phys. Chem. Chem. Phys.*, 2015, **17**, 10028-10039.
55. R. T. Haasch, E. Breckenfeld and L. W. Martin, *Surf. Sci. Spectra*, 2014, **21**, 87-94.
56. A. B. Posadas, A. O'Hara, S. Rangan, R. A. Bartynski and A. A. Demkov, *Appl. Phys. Lett.*, 2014, **104**, 092901.
57. M. Aufray, S. Menuel, Y. Fort, J. Eschbach, D. Rouxel and B. Vincent, *J. Nanosci. Nanotechnol.*, 2009, **9**, 4780-4785.
58. J. Seo, T. Hisatomi, M. Nakabayashi, N. Shibata, T. Minegishi, M. Katayama and K. Domen, *Adv. Energy Mater.*, 2018, **8**, 1800094.
59. K. Isawa, R. Itti, J. Sugiyama, N. Koshizuka and H. Yamauchi, *Phys. Rev. B*, 1994, **49**, 3534.
60. S. Shibagaki and K. Fukushima, *J. Eur. Ceram. Soc.*, 1999, **19**, 1423-1426.
61. J.-C. Dupin, D. Gonbeau, P. Vinatier and A. Levasseur, *Phys. Chem. Chem. Phys.*, 2000, **2**, 1319-1324.
62. H. Tan, Z. Zhao, W.-b. Zhu, E. N. Coker, B. Li, M. Zheng, W. Yu, H. Fan and Z. Sun, *ACS Appl. Mater. Interfaces*, 2014, **6**, 19184-19190.
63. K. Conder, E. Pomjakushina, A. Soldatov and E. Mitberg, *Mater. Res. Bull.*, 2005, **40**, 257-263.
64. M. Karppinen, M. Matvejeff, K. Salomäki and H. Yamauchi, *J. Mater. Chem.*, 2002, **12**, 1761-1764.
65. S. Roh, S. Lee, M. Lee, Y.-S. Seo, A. Khare, T. Yoo, S. Woo, W. S. Choi, J. Hwang and A. Glamazda, *Phys. Rev. B*, 2018, **97**, 075104.
66. Y. G. Abreu, J. C. Soares, R. L. Moreira and A. Dias, *J. Phys. Chem. C*, 2016, **120**, 16960-16968.
67. D. A. Tenne, A. Farrar, C. Brooks, T. Heeg, J. Schubert, H. Jang, C. Bark, C. Folkman, C. Eom and D. Schlom, *Appl. Phys Lett.*, 2010, **97**, 142901.
68. R. Ouillon, J. Pinan-Lucarre, P. Ranson, P. Pruzan, S. K. Mishra, R. Ranjan and D. Pandey, *J. Phys.: Condens. Matter*, 2002, **14**, 2079.
69. G. Jyothi, L. S. Kumari and K. Gopchandran, *RSC Adv.*, 2017, **7**, 28438-28451.
70. T. Hirata, K. Ishioka and M. Kitajima, *J. Solid State Chem.*, 1996, **124**, 353-359.
71. J. M. Jehng and I. E. Wachs, *Chem. Mater.*, 1991, **3**, 100-107.
72. D. Music, P. Schmidt and S. Mráz, *J. Vac. Sci. Technol. A,* 2017, **35**, 061512.
73. P. Darapaneni, N. S. Moura, D. Harry, D. A. Cullen, K. M. Dooley and J. A. Dorman, *J. Phys. Chem. C*, 2019, **123**, 12234-12241.

Table of Content Graphic

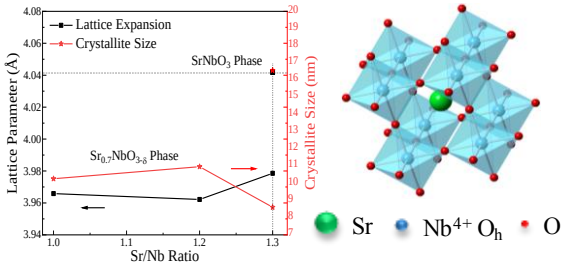

Crystallization of $Sr_{1-x}NbO_{3-\delta}$ nanoparticle using the low-pressure wet-chemical method.